Transformation-Induced Microcracks and Their Arrest with Different Deformation Temperatures in a Medium Mn Steel

YUTAO ZHOU, MOTOMICHI KOYAMA, TOMOHIKO HOJO, SAYA AJITO, and EIJI AKIYAMA

In the present study, the temperature dependence of microstructure and damage evolution in the medium Mn steel was investigated by tensile testing and microstructure examinations to explain the damage and fracture mechanisms. The flow behavior with serrations and work hardening rate were significantly affected by the deformation temperatures ranging from 173 K to 373 K (− 100 °C to 100 °C). Moreover, ultimate tensile strength, uniform elongation and total elongation showed significant temperature dependence. Deformation-induced martensite acted as the initiation site of damage. Accordingly, the critical strain for damage initiation and associated damage initiation probability decreased with decreasing deformation temperature due to the combined effect of the increase in flow stress and the decrease in the retained austenite stability. Furthermore, the decrease in deformation temperature strongly deteriorated the micro-damage arrestability of ferrite, which was attributed to increasing flow stress or stress intensity factor for brittle cracking after martensite cracking, resulting in fracture mode transition from ductile to quasi-cleavage fractures.

I. INTRODUCTION

WITH the improvement of sustainability of structures, advanced high strength steels (AHSS), especially medium Mn (3 to 12 mass pct Mn) steels in AHSS, have drawn attention as high performance structural parts for automotive, cryogenic and other applications.[1–4] These key structural parts require not only good balance of strength and ductility, but also high damage tolerance under various loading and temperature condition.[5–7] Therefore, it is important to understand the microstructure and associated damage evolution of the medium Mn steels in a specific deformation process.

Numerous studies on the medium Mn steels have mainly focused on the influences of alloy design and thermomechanical process on microstructural control and mechanical properties at room temperature within the past decade.[8–11] All these studies have reached a consensus, namely, the high strength is attributed to the ultrafine-grained matrix structure, while the excellent ductility is owing to deformation-induced martensitic transformation and/or deformation twinning, i.e., transformation-induced plasticity (TRIP) and or twinning-induced plasticity (TWIP) mechanisms.[12–15] In addition, great efforts have been made to reveal the effect of the characteristics of retained austenite on the martensitic transformation from retained austenite.[12,16–20] However, there is a contradictory conclusion in terms of the effect of deformation-induced martensite on the micromechanical behavior. Several studies[21,22] revealed that the fracture strain decreased with martensitic transformation of retained austenite, which would result from microscopic stress/strain concentration. These facts suggest that the martensitic transformation can cause micro-cracking during plastic deformation and therefore reduces the fracture resistance particularly when a large strain over uniform elongation (UEl) is provided. Moreover, some reports[23,24] also investigated strain and elemental partitioning among multiple microstructure constituents of the medium Mn steels to uncover unique micromechanical behavior. Although these studies have

YUTAO ZHOU is with the Institute for Materials Research, Tohoku University, Katahira 2-1-1, Aoba-ku, Sendai, Miyagi, 980-8577 Japan and also with the Graduate School of Engineering, Tohoku University, Aramaki Aza Aoba, Aoba-ku, Sendai, Miyagi, 980-8579 Japan. MOTOMICHI KOYAMA, TOMOHIKO HOJO, SAYA AJITO and EIJI AKIYAMA are with the Institute for Materials Research, Tohoku University. Contact e-mail: motomichi.koyama.c5@tohoku.ac.jp; tomohiko.hojo.a1@tohoku.ac.jp

reported the fracture behavior of medium Mn steels at room temperature, as well as abundant micromechanical modeling works, temperature effects on deformation and damage evolution behaviors and their mechanisms have not been systematically investigated so far.

Besides, several studies reported that the medium Mn steel is a promising candidate material for cryogenic applications owing to the superior impact toughness.[25–30] Han et al.[26] reported that cold-rolling and subsequent annealing of Fe–7Mn–0.1C–0.5Si (in wt pct) steel, which resulted in fine and granular austenite, enhanced a low temperature fracture resistance through the elimination of solute segregation at the prior grain boundaries. Kim et al.[28] reported that an Fe–8Mn–0.2C steel with the triplex-phase microstructure exhibited different impact toughness depending on the amount of δ ferrite, the retained austenite stability, and the size of prior austenite grains. Kuzmina et al.[29] pointed out that retained austenite improved the toughness in Fe–9Mn alloy owing to that austenite reverted-transformation cleans the interfaces from Mn by partitioning the Mn into the fresh austenite. Meanwhile, Chen et al.[30] suggested that the effect of retained austenite on tensile and impact properties of Fe–5Mn–0.04C steel is dependent on austenite morphology and associated phase stability. Because behaviors of martensitic transformation and deformation twinning are significantly dependent on the deformation temperature, a different scenario may arise at deformation temperatures different from room temperature to understand the excellent resistance to cryogenic fracture. Hence, there are still a lot of challenges in multiphase steels compared with fully face-centered cubic (FCC) alloys such as TWIP steels,[31–33] austenitic stainless steels,[34–36] nickel-based alloys,[37,38] and a group of high entropy alloys.[39–41] Accordingly, their detailed microstructures or deformation mechanisms of the cold-rolled and annealed medium Mn steels at different deformation temperatures still need to be further studied.

Therefore, we selected Fe–5Mn–0.1C steel, as a representative medium Mn steel firstly developed by Miller due to the following reasons.[42] (1) The excellent combination of strength and ductility/toughness can be obtained in Fe–5Mn–0.1C steel through simple heat treatment such as intercritical annealing. (2) Fe–5Mn–0.1C steel with some minor elements show a reasonable material cost, which has received much attention as third generation AHSS. In particular, Mn is most attractive as a substitute for Ni and similar effect on phase transformation. The objective of the present study is to elucidate the temperature effects on microstructure-dependent damage behaviors in a medium Mn steel. In particular, the damage evolution associated with martensitic transformation was systematically investigated. On that basis, it is shown that how the deformation temperature is significant regarding microstructural damage evolution and the associated fracture behavior of the medium Mn steel.

II. EXPERIMENTAL PROCEDURE

A. Materials

A medium Mn steel with a nominal composition of Fe–5Mn–0.1C (wt pct) was fabricated by vacuum induction melting. The detailed composition is listed in Table I. The ingot was homogenized at 1473 K (1200 °C) for 1 hour, and hot-rolled to an 8 mm thick plate at a temperature above 1123 K (850 °C). The hot-rolled plate was cold-rolled to about a 2-mm thin sheet with a thickness reduction of about 75 pct. Then the cold-rolled sheet was intercritically annealed at 923 K (650 °C) for 30 minutes and finally cooled to room temperature in the ambient atmosphere. The obtained microstructure obtained by electron channeling contrast imaging (ECCI) and an electron backscatter diffraction (EBSD) measurement showed fully recrystallized grains (Figure 1(a)), and a dual phase microstructure consisting of ferrite and retained austenite (Figure 1(c)). The conditions for ECCI and EBSD are shown later.

B. Tensile Test

Tensile specimens with gauge dimensions of 25 mm in length, 2 mm in width, and 1 mm in thickness were produced by electric discharge machining along the rolling direction. The specimens were mechanically polished by abrasive papers before the tensile test. The uniaxial tensile tests were performed at an initial strain rate of 1×10^{-4} s^{-1} at 173 K, 243 K, 297 K and 373 K (-100 °C, -30 °C, 24 °C and 100 °C) using a tensile testing machine equipped with a thermostatic chamber as illustrated in Figure 2. The strain at the gauge part of specimens was measured using a video extensometer. Total elongation (TEl) was determined by measuring the gauge lengths before and after the test.

C. Microstructure and Damage Characterization

Microstructures before and after tensile deformations were characterized by EBSD and ECCI. Specimens for EBSD and ECCI were mechanically polished using the abrasive papers, 9 and 3 μm single crystalline diamond slurries and colloidal silica with a particle diameter of 60 nm. The EBSD analyses were performed at an accelerating voltage of 20 kV, a working distance of approximately 15 mm. The data were then analyzed by TSL OIM analysis software. The ECCI was conducted at an acceleration voltage of 30 kV and a working distance of 5 mm. Meanwhile, damage quantification was conducted using a series of scanning electron microscope (SEM) images of the fractured specimens containing damages such as cracks and voids. The contrast of these images was binarized, and then the amount of damage that appears as black was quantified as the area fraction and number of damages as schematically shown in Figure 3. The three parameters considered for damage evaluation were damage area

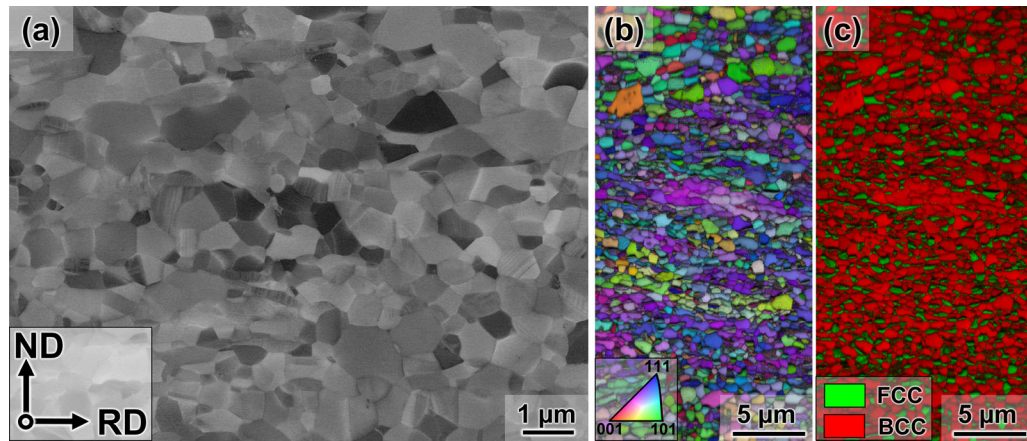| Alloy	C	Si	Mn	S	Al	O	N	Fe
Fe–5Mn	0.092	0.04	4.91	0.002	0.024	0.005	0.001	Bal.

Fig. 1—As-annealed microstructure of the medium Mn steel. (*a*) ECC image, (*b*) RD-inverse pole figure (IPF) map with image quality (IQ), and (*c*) phase map with IQ. ND and RD represent the normal direction and rolling direction, respectively.
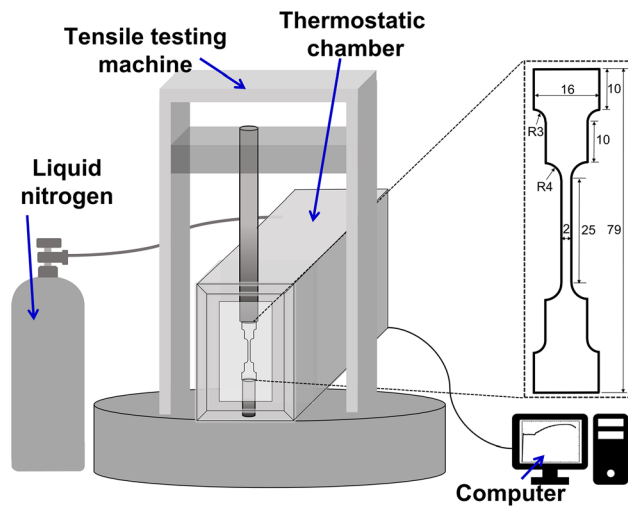

Fig. 2—Configuration of tensile testing apparatus.

Fig. 3—A schematic diagram of the quantitative analysis of damage evolution.

fraction, number density, and average damage size.[43–45] The damage area fraction (*D*) is defined as

$$D = A_d/A_a \qquad [1]$$

where A_d is the damaged cross-sectional area and A_a is the area of the entire region under observation. The number of damage incidents per area (*n*) is defined as

$$n = N/A_a \qquad [2]$$

where *N* is the number of damages for each region. The average damage size (d_{ave}) is defined as
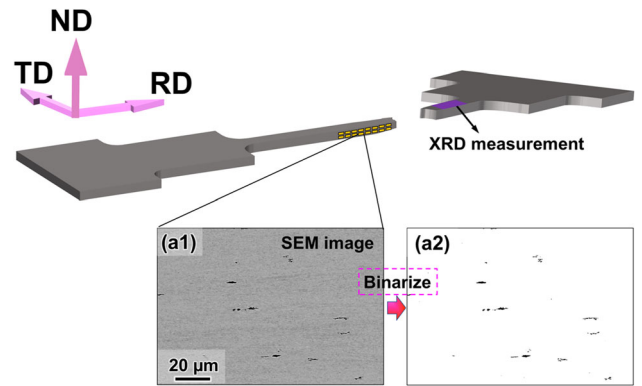
$$d_{ave} = D/n \qquad [3]$$

The quantitative damage evolution behavior was evaluated by plotting these values against the local strain. The local strain (*ε*) at the damaged area was defined by the following equation:[46]

$$\varepsilon = \ln \frac{t_0}{t} \qquad [4]$$

where t_0 and *t* are the initial thickness, and the local thickness at the observed point after the fracture, respectively.

To quantitatively evaluate the strain of the region used for the XRD analysis, the portion of the specimens containing strain gradients were excluded for the measurements. That is, the uniformly deformed portion of the specimen, whose strain corresponds to uniform elongation, was used. X-ray diffraction (XRD) analyses

were conducted for the uniformly deformed part of the fractured tensile specimen after electropolishing in a solution of 10 pct perchloric acid and 90 pct acetic acid at 20 V for 120 seconds. The volume fractions of retained austenite before and after tensile deformation were measured using XRD with a copper target at 40 kV and 15 mA and a nickel filter at integrated intensities of $(200)\alpha$, $(211)\alpha$, $(200)\gamma$, $(220)\gamma$, and $(311)\gamma$ peaks. The peak fitting of each diffraction peak was conducted using HighScore software. The 2θ scanning range, 2θ step size for each measurement were 40 to 100 deg, and 0.04 deg, respectively. Then, the volume fraction of retained austenite was evaluated based on the peak profile.[47] All XRD measurements were carried out three times to ensure reproducibility.

III. RESULTS

A. Mechanical Properties

Figures 4(a) and (b) show engineering stress–strain curves and corresponding tensile properties obtained at different temperatures. Discontinuous yielding and Lüders elongation appeared, irrespective of deformation

temperature. The Lüders elongation increased with increasing deformation temperature. As reported,[48–50] serrations stemming from Portevin–Le–Châtelier (PLC) effect were observed. Figure 4(b) shows that ultimate tensile strength (UTS) decreased with increasing temperature, whereas yield strength (YS) was approximately 660 MPa. In addition, UEl and TEl increased with increasing deformation temperature. In particular, when the temperature increased from 297 K to 373 K (24 °C to 100 °C), the UEl and TEl significantly increased from 22 to 36 pct and from 25 to 40 pct, respectively.

Figures 4(c) and (d) show the working hardening rate curves. The obvious serration of working hardening rate at 173 K (− 100 °C) may be attributed to the deformation temperature instability. All the specimens exhibited the fracture after Considère criterion was satisfied (i.e., $\sigma > d\sigma/d\varepsilon$ where σ and ε indicate true stress and strain).[51] The work hardening behavior can be separated into two stages: (1) the work hardening rate remains nearly constant, which corresponds to Lüders elongation, and (2) the work hardening rate again decreases with strain. The first stages exhibited no obvious change by varying deformation temperature. In the two stage, the work hardening rate decreased with increasing temperature.
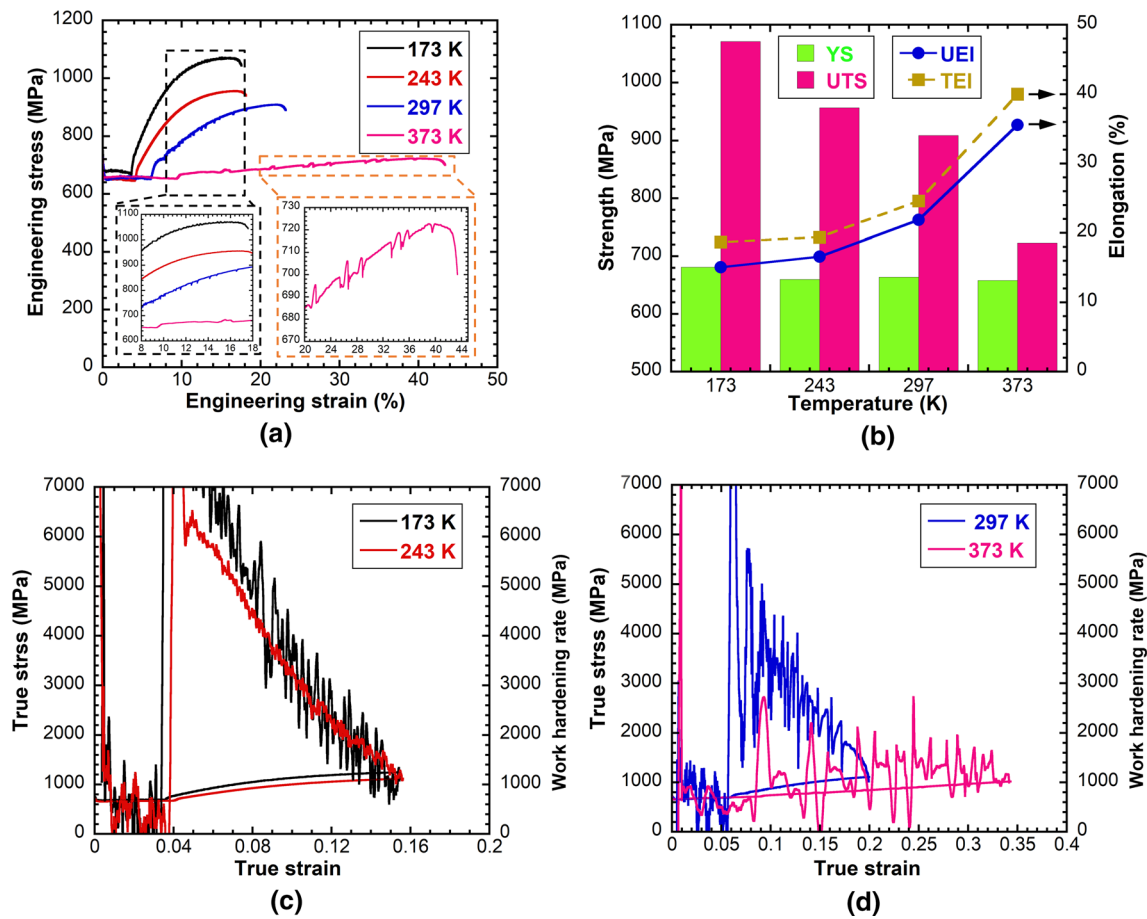

Fig. 4—Tensile behavior of the specimens at different temperatures. (a) Engineering stress–strain curves. (b) YS, UTS, UEl and TEl. (c, d) Work hardening behavior at 173 K and 243 K (− 100 °C and − 30 °C), 297 K and 373 K (24 °C and 100 °C).

B. *Martensitic Transformation Behavior*

The martensite start (*M*s) temperature was calculated using Eq. [5]:[52]

$$M_s\left(^{\circ}C\right) = 475.9 - 335.1C - 34.5Mn - 1.3Si \\ + 11.67 \ln(d\gamma). \quad [5]$$

For this study, the C concentration of ferrite was set to be zero by assuming that all the carbon was partitioned into austenite. The Mn content of retained austenite was assumed to be 7.7 wt pct based on a previous study[19] that used a steel with the similar chemical composition and heat treatment. The Si content was assumed to be the same as the nominal chemical composition. The retained austenite grain size ($d\gamma = 0.14~\mu$m) was measured by EBSD *via* intercept lengths method. As a result, the M_S temperature of retained austenite was calculated as approximately 289 K (16 °C).

Figure 5 shows XRD patterns and volume fraction of retained austenite before and after the tensile tests at each temperature. The volume fraction of the retained austenite after immersion into liquid nitrogen was slightly decreased compared with that before immersion. The austenite fraction in the as-annealed specimen was 18 ± 2 pct. The austenite fractions after the tests at 173 K and 243 K (− 100 °C and − 30 °C) were lower than 1 pct, and the austenite fraction increased with increasing temperature.

Figure 6 shows the EBSD results of the specimen tested at 173 K (− 100 °C). The retained austenite transformed to martensite at the various local strains. Deformation-induced martensite was observed as low IQ value region (Here, the unindexed and low IQ value regions would have included austenite that partially transformed martensite. Such austenite is small and contains significant lattice distortion near the martensite/austenite interface, which can reduce the quality of Kikuchi-like patterns.). In addition, the KAM value, which corresponds to geometrically necessary dislocation density,[53] increased with strain. The KAM value was obtained as the average misorientation angle between measurement point and the nearest neighbor

points. When tested at 373 K (100 °C), the specimen showed that a significant amount of austenite remained even after the fracture (Figure 7). Furthermore, at the same local strain, the average KAM values of the specimen tested at 373 K (100 °C) was lower than those at 173 K (− 100 °C) particularly after the significant plastic deformation, which was probably due to lower fraction of deformation-induced martensite. It is also noteworthy that the low IQ value region, *i.e.*, martensite, showed elongated shape after the significant evolution of plasticity over 0.4, resulting in a laminated microstructure, irrespective of deformation temperature.

Figure 8 shows the distribution of ferrite texture in initial microstructure and the specimen tested at 173 K and 373 K (− 100 °C and 100 °C). the ferrite texture shifted towards the orientation ⟨101⟩ after deformation. In addition, Figure 9 shows ECC images of deformation microstructure near fracture surface in specimens deformed at (a) 173 K (− 100 °C) and (b) 373 K (100 °C). No deformation twinning was observed, irrespective of deformation temperature.

C. *Damage Evolution*

Figure 10 shows cross-sectional SEM images of the fractured specimens. All specimens possessed necking with the macroscopic scale even if the specimens were deformed at cryogenic temperatures. However, the different facets were clearly found in the fracture surfaces of specimens. Especially the sample tested at the deformation temperature of 173 K (− 100 °C) exhibited cracks that propagated parallel to the tensile direction with a length of approximately one millimeter. In addition, damages such as cracks and voids were observed particularly near the fracture surface.

Figure 11 shows fractographs obtained at the different deformation temperatures. The fracture surface obtained at 173 K (− 100 °C) showed flat facets and step-like ridges as the predominant feature (Figures 11(a1) through (a4)). The inclusions could act as a initiation site of the cleavage fracture as shown in Figure 11(a4). The inclusions are mainly oxide
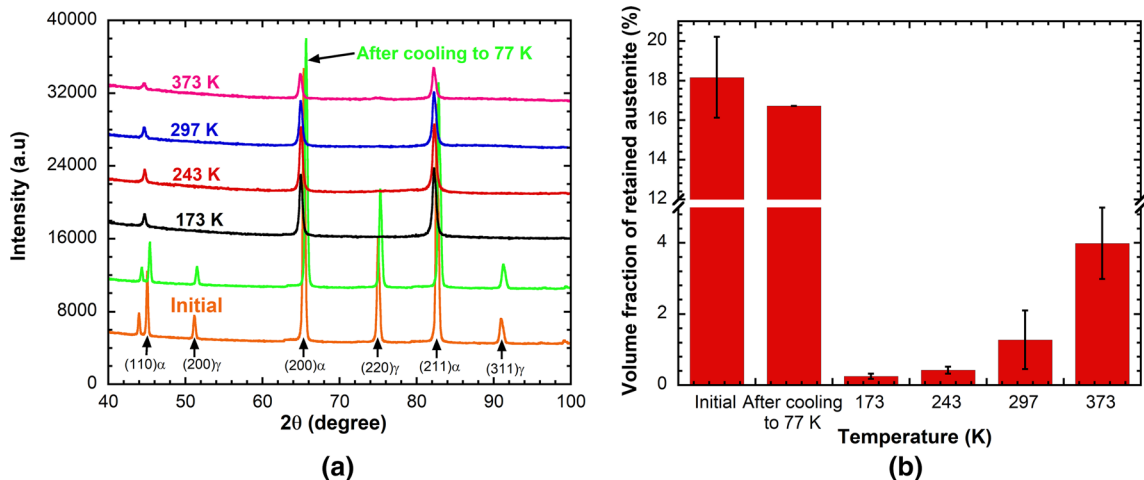

Fig. 5—(*a*) XRD patterns and (*b*) volume fraction of retained austenite before and after the tensile tests at different temperatures.
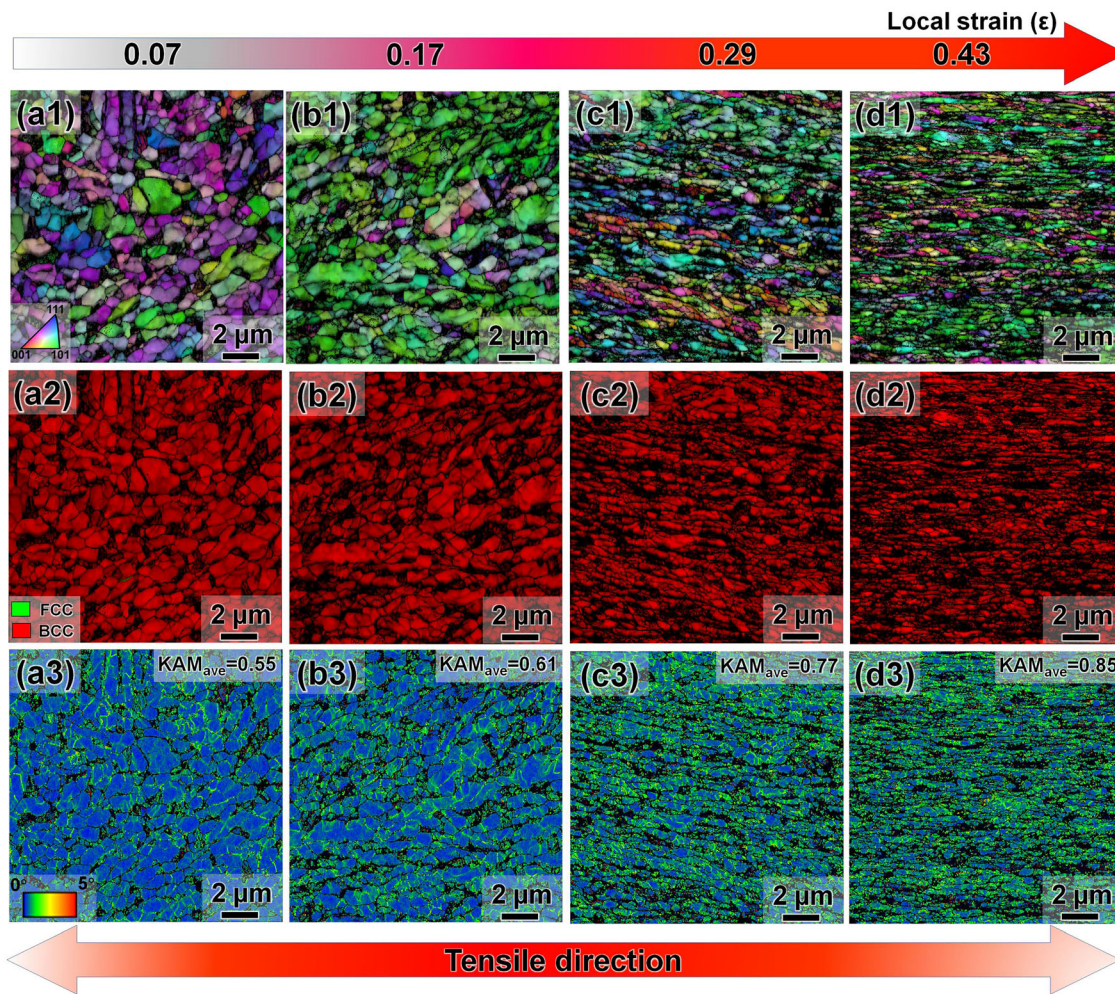
Fig. 6—EBSD maps of the deformed microstructure of deformation temperature of 173 K (− 100 °C) at the various local strain. (*a1, b1, c1, d1*) IPF map with IQ, (*a2, b2, c2, d2*) phase map with IQ, and (*a3, b3, c3, d3*) KAM map. The percentage shown in the phase maps indicates the area fraction of each phase. KAM$_{ave}$ indicates average KAM value for each image.

inclusions (*e.g.*, Al$_2$O$_3$) formed by oxygen in the molten steel and deoxidizers such as Al in the deoxidation process, and some MnS inclusion was formed during solidification based on the high Mn content in the molten steel.[5] Fracture surface obtained at 243 K (− 30 °C) showed a mixture of brittle and ductile features (Figures 11(b2) through (b4)) consisting of the similar brittle feature to that at 173 K (Figures 11(a2) and (b2)) and a significant portion showed dimples as well (Figure 11(b3)). When the temperature was set to 297 K and 373 K (24 °C and 100 °C), the fracture surface exhibited typical ductile fracture mode with dimples. There were two types of dimples as shown in Figures 11(c2) and (d3). The first type is deep dimples with fisheye, which was formed via voids or crack formation at the matrix/inclusion interfaces.[46] The second type is shallow dimples without a fisheye.

The damage area fraction, number density of damage, and average damage size at various local strains were measured as shown in Figure 12. The area fraction (Figure 12(a)) and number density of damage (Figure 12(b)) decreased with increasing deformation

temperature. Since the number density of damage at around the zero strain and subsequent plateau stage correspond to the number density of pre-existing defects such as inclusions, the critical strain for deformation-induced damage initiation at 373 K is larger than 0.2. The critical strain for damage initiation decreased when the temperature was decreased to 297 K and lower. In contrast, the average damage size after the damage initiation (over 0.2 strain) did not show a significant change against deformation temperature, *i.e.*, a range of 1.5 to 2.1 μm^2 (Figure 12(c)). Assuming that the damage shape is spherical, the damage diameter is 1.2 to 1.5 μm, which approximately corresponds to the size of coarse retained austenite grains as shown in Figure 1.

Figure 13 shows damage in the specimens tested at 297 K (24 °C). The primary damage initiation site was deformation-induced martensite that appeared as the low IQ region. The damage was arrested at ferrite grains as shown in Figures 13(a) through (c). Figures 14(a) and (b) show the damage of the specimen deformed at 243 K (− 30 °C). The damage initiation site was martensite or the ferrite/martensite interface (Figures 14(c) and (d)).
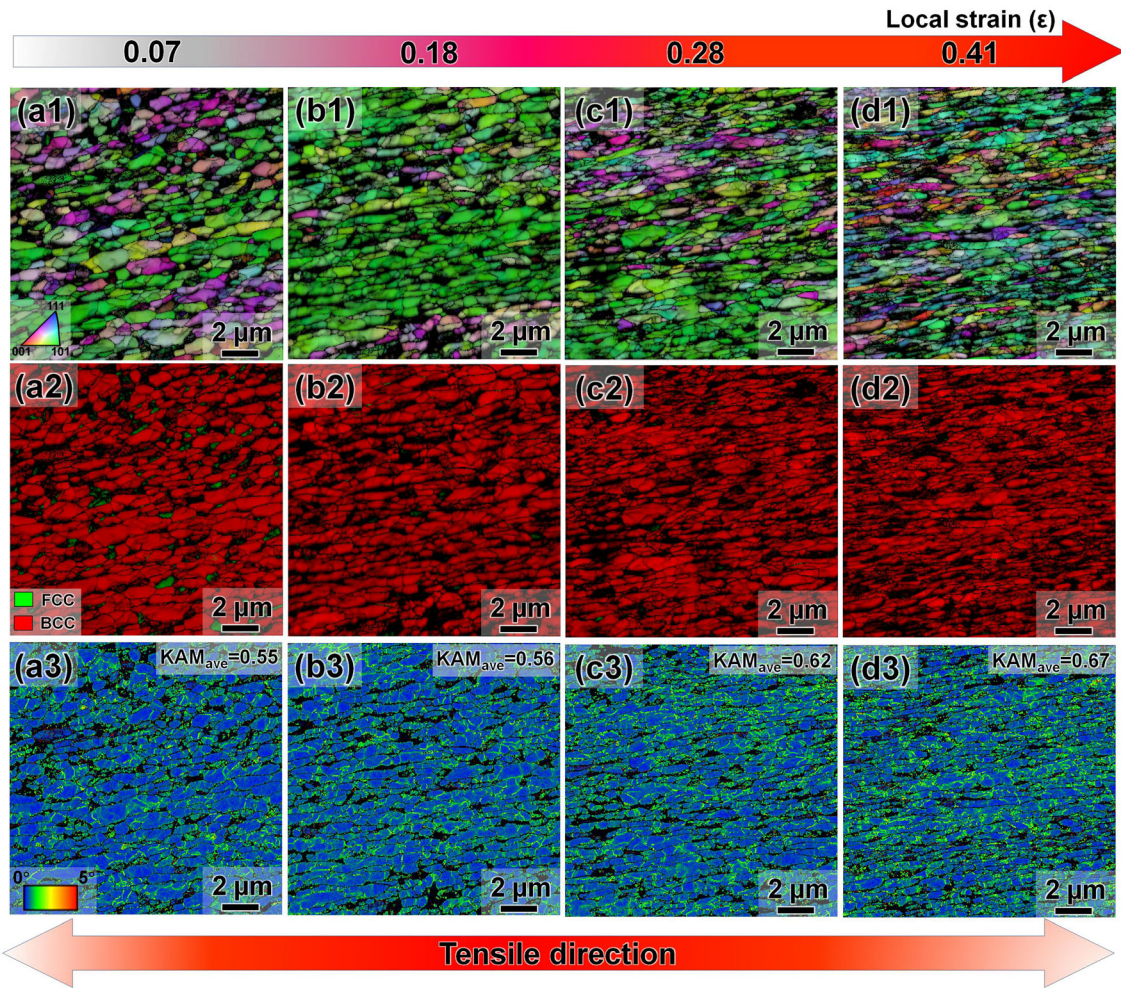
Fig. 7—EBSD maps of the deformed microstructure of tensile temperature of 373 K (100 °C) at the various local strain. (*a1, b1, c1, d1*) IPF map with IQ, (*a2, b2, c2, d2*) phase map with IQ, and (*a3, b3, c3, d3*) KAM map. KAM$_{ave}$ indicates average KAM value for each image.
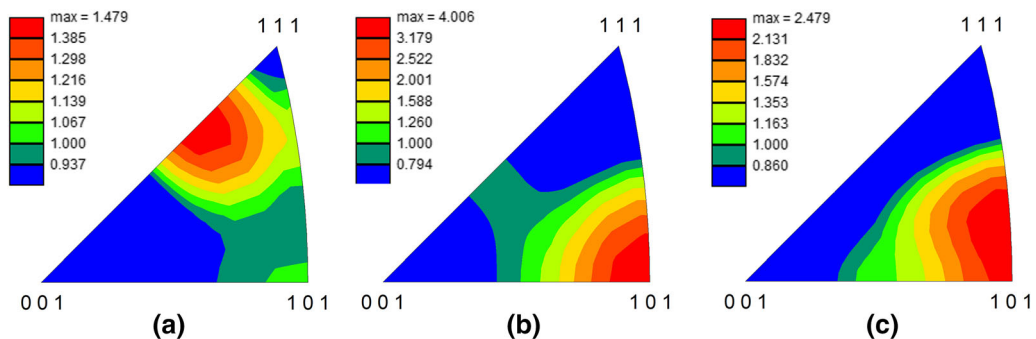

Fig. 8—Distribution of ferrite texture in (*a*) initial microstructure, (*b*) the deformed microstructure of tensile temperature of 173 K (− 100 °C) in local strain of 0.43, and (*c*) the deformed microstructure of tensile temperature of 373 K (100 °C) in local strain of 0.41.

The damage tip was blunted by the plastic deformation of ferrite even at the low temperature (Figure 14(e)).

Even at 173 K (− 100 °C), the initiation site (martensite) and arrest site (ferrite) did not change. However, crack propagation along the tensile direction occurred abnormally as shown in Figure 15(a). The crack tip was blunted with bright contrast as shown in Figure 15(a). Some branched cracks were found as seen in

Figures 15(b) through (d). Figure 15(e) shows an example of the crack initiation site at 173 K. Because the provided strain was small compared to the other temperature conditions, martensite around the small crack was clearly identified as low IQ regions (Figure 15(f)) with the lath morphology (Figure 15(g)) and the body-centered cubic structure (Figure 15(h)).
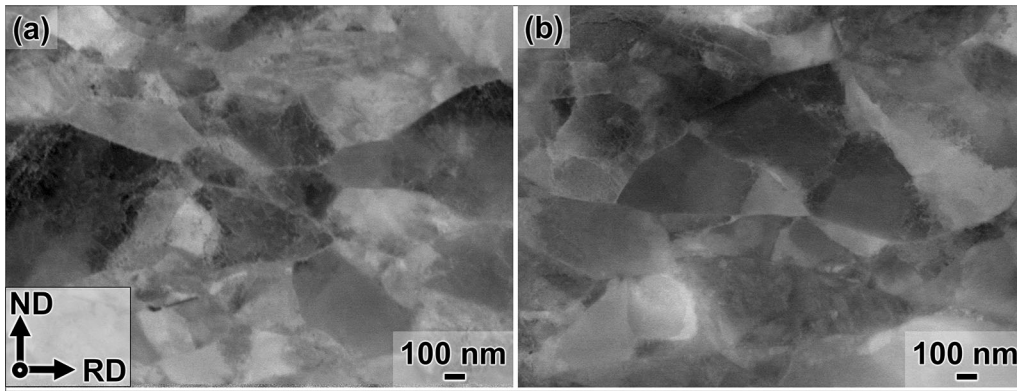
Fig. 9—ECC images of deformation microstructure near fracture surface in specimens deformed at (*a*) 173 K (− 100 °C) and (*b*) 373 K (100 °C).
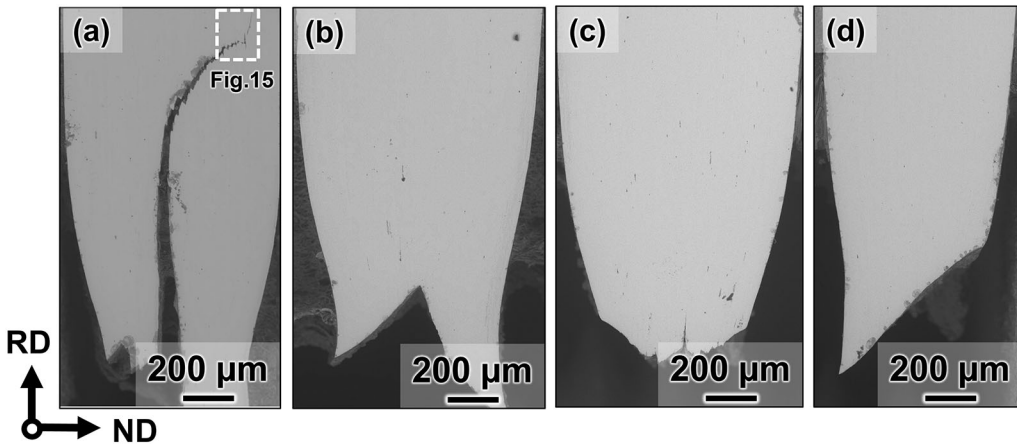

Fig. 10—SEM images showing damages near the fractured surface of the specimens tested at (*a*) 173 K (− 100 °C), (*b*) 243 K (− 30 °C), (*c*) 297 K (24 °C), and (*d*) 373 K (100 °C).

According to Figures 15(g) and (h), the cracks formed along the ferrite/martensite interface.

IV. DISCUSSION

A. *Temperature Dependence of Deformation Microstructure*

As mentioned above, the deformation temperature has a significant influence on the transformation behavior of retained austenite during plastic deformation. More specifically, the martensitic transformation occurs via the crystallographic change sequence: $\gamma \rightarrow \varepsilon \rightarrow \alpha'$.[54] Because the γ–ε martensitic transformation originates from motion of Shockley partials, stacking fault energy (SFE) is an important factor determining the plasticity mechanism.[55] In addition to the martensitic transformation, multiple plasticity mechanisms such as extended dislocation glide and deformation twinning can also be discussed comprehensively in austenite with a low SFE.[56,57] To analyze the plasticity mechanism at different deformation temperatures for the retained austenite, the Olson–Cohen thermodynamic model was adopted to calculate the SFE as expressed in the following equation:[58]

$$\mathrm{SFE} = 2\rho\Delta G^{\gamma\rightarrow\varepsilon} + 2\sigma_{\gamma/\varepsilon} \quad [6]$$

where ρ, $\Delta G^{\gamma\rightarrow\varepsilon}$ and $\sigma_{\gamma/\varepsilon}$ represent the molar surface density along {111} planes, difference in the molar Gibbs free energy between the austenite and ε-phase, and the interfacial energy per unit area of the phase boundary, respectively. $\sigma_{\gamma/\varepsilon}$ is assumed to be 8 mJ/m² .[59]

Table II lists the thermodynamic values and functions used to calculate the SFE. Here, the chemical composition of the retained austenite was assumed to be Fe–7.7Mn–0.51C in wt pct. Figure 16 shows SFE value vs. temperature for the retained austenite. It is obvious that SFE increased with increasing temperature. The SFEs at 173 K, 243 K, 297 K, and 373 K (− 100 °C, − 30 °C, 24 °C, and 100 °C) were calculated to be − 21.9, − 13.2, − 2.3, and 14.8 mJ/m², respectively. The SFE at the temperature ranging from 173 K to 297 K (− 100 °C to 24 °C) was negative, which implies the presence of significant thermal driving force for spontaneous martensitic transformation. However, a large amount of austenite remained even in the cryogenic temperature, which is owing to the geometrical
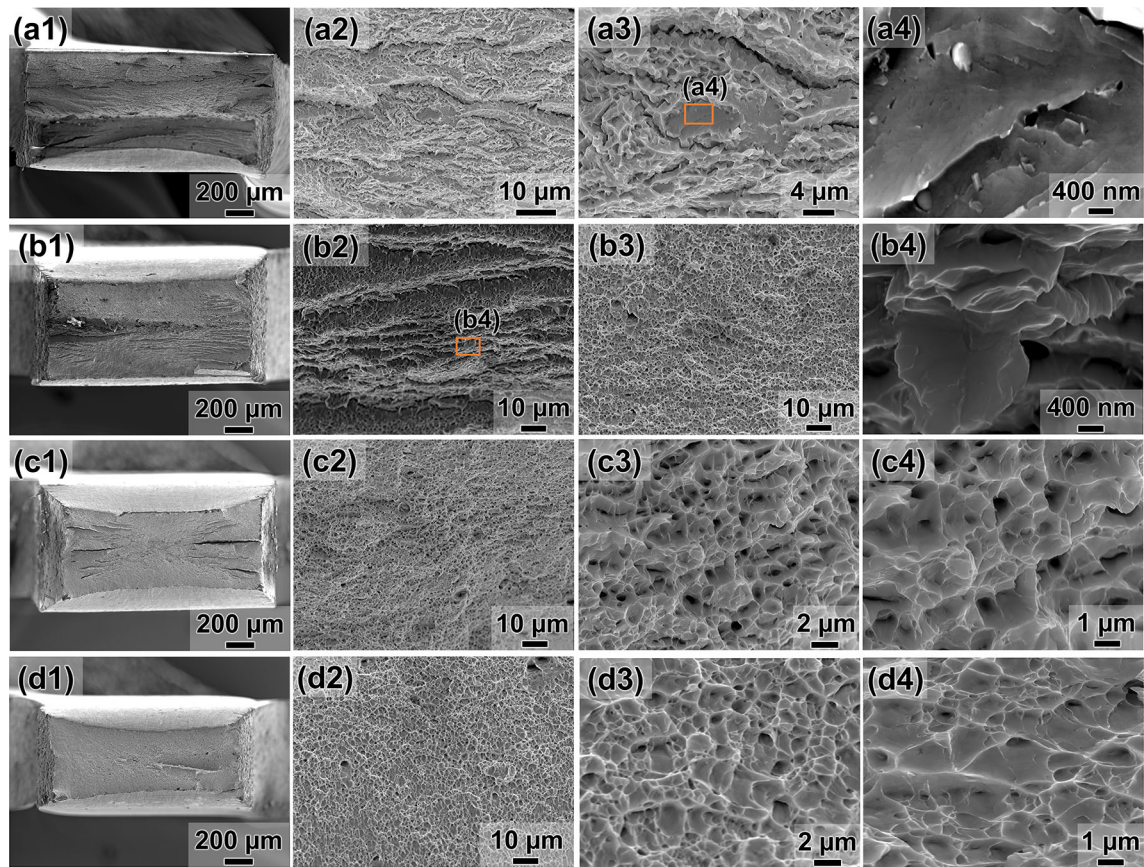
Fig. 11—Fracture surfaces of the specimens tested at (*a1, a2, a3, a4*) 173 K (− 100 °C), (*b1, b2, b3, b4*) 243 K (− 30 °C), (*c1, c2, c3, c4*) 297 K (24 °C), and (*d1, d2, d3, d4*) 373 K (100 °C).

constraint effect in the fine-grained microstructure.[62] Therefore, a slight help of deformation caused the martensitic transformation particularly at the cryogenic temperatures, which resulted in high work hardening rate. The SFE at 373 K (100 °C) was positive but still below 20 mJ/m^2. Generally, the deformation-induced martensitic transformation can occur when the SFE is below 20 mJ/m^2, which is consistent with the present result that the deformation-induced martensitic transformation occurs even at 373 K (100 °C) (Figure 7). Any deformation twin plates, which appear in low SFE materials, were not observed (Figure 9). It is also noteworthy that, although ε-martensite was not observed for the fractured tensile specimens (Figures 6 and 7), a significant amount of ε-martensite was observed at a tensile strain of 5 pct in the previous study.[63] These results indicate that the martensitic transformation occurred with the sequence of $\gamma \rightarrow \varepsilon \rightarrow \alpha'$.

B. Temperature Dependence of Fracture Behavior

The dependence of UTS on deformation temperature was significantly higher than that of YS, which can be attributed to the TRIP effect. Namely, the stability of retained austenite decreased with decreasing deformation temperature (Figure 5), which promoted the occurrence of deformation-induced martensitic transformation. However, the TRIP effect promoted by decreasing temperature did not increase the UEl. In general, UEl is determined by critical conditions for the occurrence of necking or premature fracture. Therefore, UEl increases when YS is low; a high work hardening rate is sustained; resistance to brittle cracking is high.[31,33] In this context, because all the fractures occurred after satisfying Considère criterion (Figures 4(c) and (d)), the occurrence of brittle cracking did not affect UEl. That is, the occurrence of early necking due to the increase in YS and decrease in work hardening rate in the late deformation stage is the major factor causing the decrease in UEl with decreasing temperature.

In terms of TEl, the difference between UEl and TEl was within 2 to 4 pct, which indicates that the final fracture occurred after only a small amount of plasticity evolution, irrespective of temperature. A cause of the low post-uniform elongation at 373 K is perhaps due to the occurrence of dynamic strain aging, which has been known as blue brittleness associated with localized plasticity.[64] On the other hand, the serrated flow associated with dynamic strain aging was suppressed when the temperature was decreased. Instead, the high flow stress and formation of hard martensite in an early deformation stage (Figures 5 and 6) assist occurrence of brittle cracking after necking. Accordingly, a considerable number of the brittle-like feature were observed at
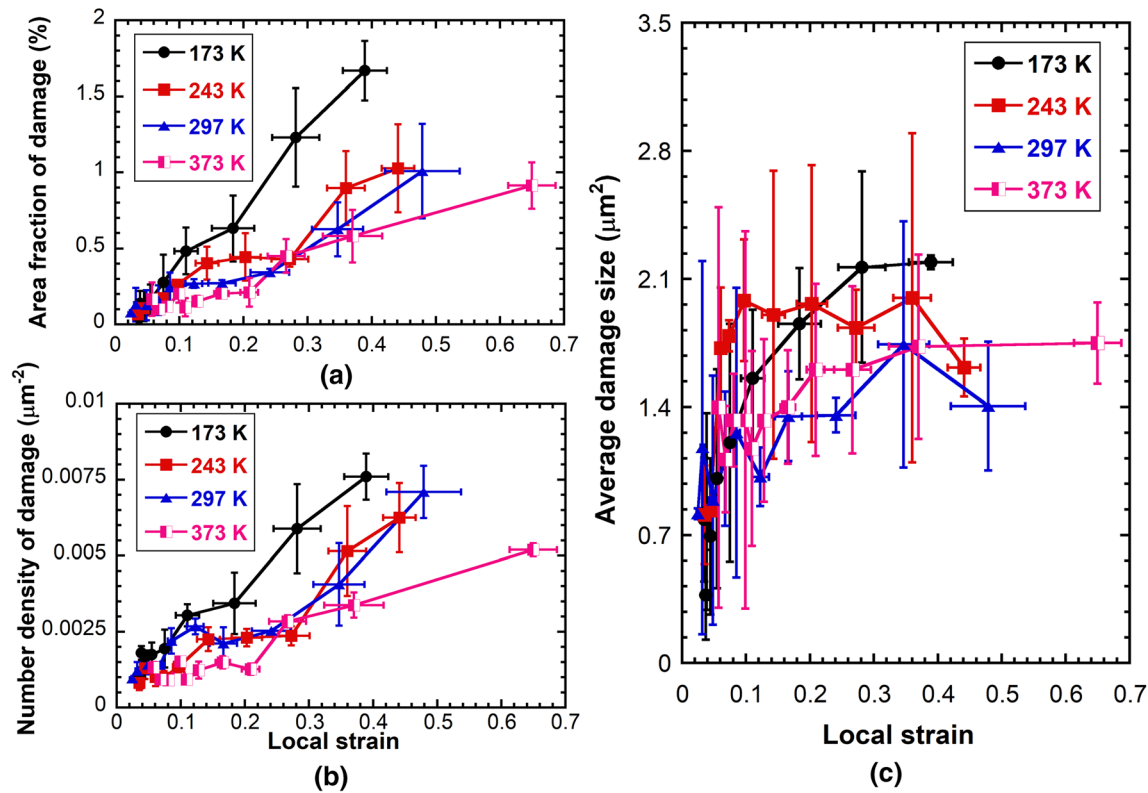
Fig. 12—(*a*) Damage area fraction, (*b*) number density of damage, and (*c*) average damage size plotted against local strain at different temperatures.
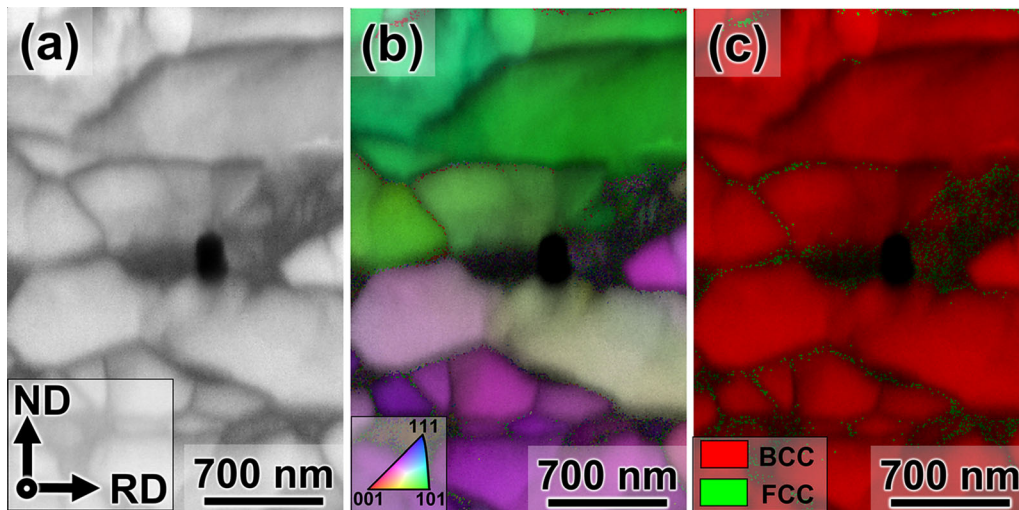

Fig. 13—EBSD maps of damage at a deformation temperature of 297 K (24 °C). (*a*) IQ map, (*b*) IPF map with IQ, and (*c*) phase map with IQ.

deformation temperatures of below 243 K (− 30 °C) as shown in Figure 11. In addition, mobility of screw dislocations in ferrite, which is predominantly controlled by thermal activation process, markedly decreases with decreasing temperature. Therefore, the crack arrestability of ferrite in the cryogenic temperature was significantly deteriorated. It is also noteworthy that a significant stress partitioning occurs in the steel consisting of soft ferrite/austenite and hard martensite. Because

a large phase stress is loaded to martensite, the martensite cracking subsequently results in rapid deformation of the soft phases surrounding the crack tip. When the soft phase such as ferrite cannot plastically accommodate the crack tip stress, brittle crack propagation occurs.[65] Thus, crack arrestability in ferrite becomes low in the cryogenic temperature, which decreased macroscopic elongation. In addition, inclusions are recognized as the general initiation site of
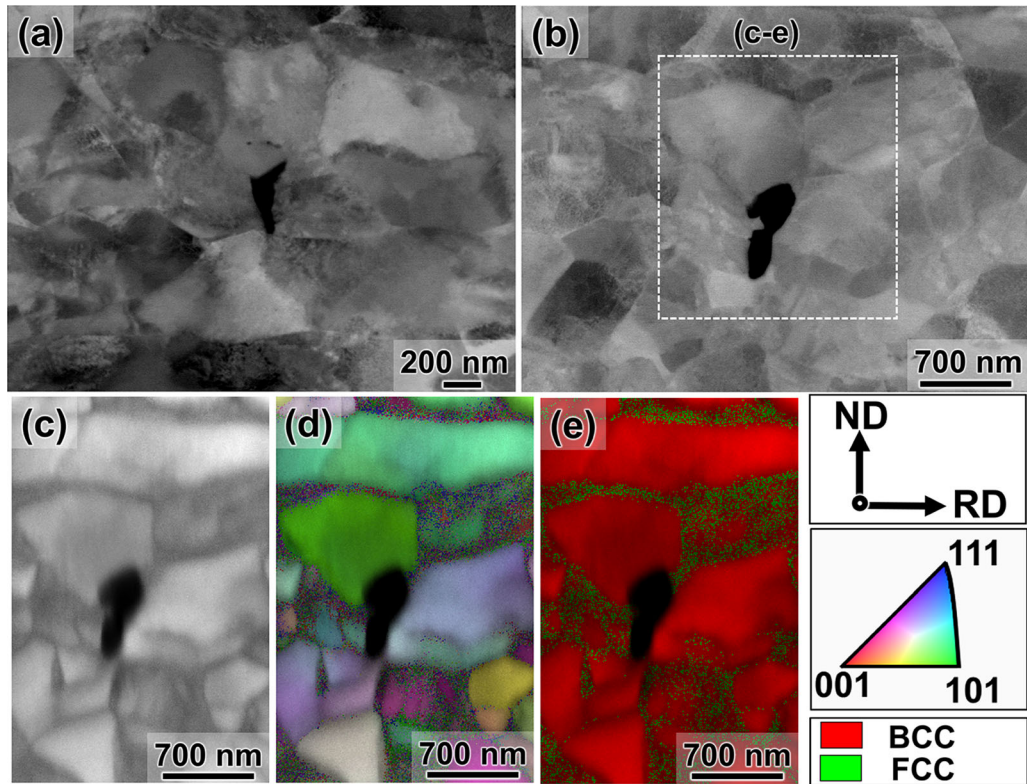
Fig. 14—(*a*) ECC images of damage at a deformation temperature of 243 K (− 30 °C), and (*b-e*) ECC images and corresponding EBSD maps of damage at a deformation temperature of 243 K (− 30 °C). (b) ECC image, (*c*) IQ map, (*d*) IPF map with IQ, and (*e*) phase map with IQ.
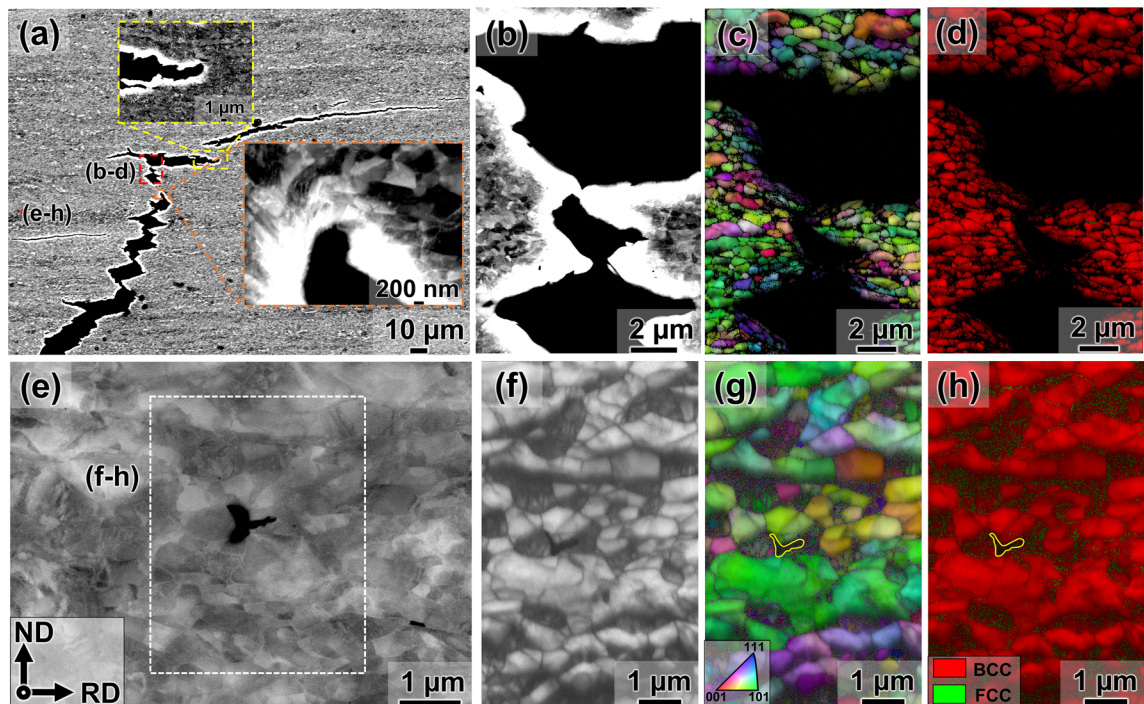

Fig. 15—ECC images and corresponding EBSD maps around cracks in specimens deformed at 173 K (-100 °C). (*a*) An overview of the ECC image of crack as marked in Figure 10(a), (*b*, *e*) magnified ECC images of the marked regions in (a), (*c*, *g*) IPF maps with IQ, (*d*, *h*) phase maps with IQ, and (*f*) IQ map.

Table II. Numerical Values and Functions Used for the Calculation SFE[59–61]

Parameter	Values and Functions (J/mol)	References
ρ	$= \dfrac{4}{\sqrt{3}a^2 N_A}$	59
$\Delta G^{\gamma \to \varepsilon}$ (J/mol)	$x_{Fe}\Delta G_{Fe}^{\gamma\to\varepsilon} + x_{Mn}\Delta G_{Mn}^{\gamma\to\varepsilon} + x_{Si}\Delta G_{Si}^{\gamma\to\varepsilon} + + x_{Al}\Delta G_{Al}^{\gamma\to\varepsilon} \; x_C \Delta G_C^{\gamma\to\varepsilon}$ $+ x_{Fe}x_{Mn}\Delta\Omega_{FeMn}^{\gamma\to\varepsilon} + x_{Fe}x_C\Delta\Omega_{FeC}^{\gamma\to\varepsilon} + x_{Fe}x_{Si}\Delta\Omega_{FeSi}^{\gamma\to\varepsilon}$ $+ x_{Fe}x_{Al}\Delta\Omega_{FeAl}^{\gamma\to\varepsilon} + x_{Mn}x_C\Delta\Omega_{MnC}^{\gamma\to\varepsilon} + \Delta G_{mg}^{\gamma\to\varepsilon}$	59
$\Delta G_{mg}^{\gamma\to\varepsilon}$	$G_{mg}^{\varepsilon} - G_{mg}^{\gamma}$	59
$\Delta G_{Fe}^{\gamma\to\varepsilon}$ (J/mol)	$-2243.38 + 4.309\,T$	59
$\Delta G_{Mn}^{\gamma\to\varepsilon}$ (J/mol)	$-1000 + 1.123\,T$	59
$\Delta G_{Al}^{\gamma\to\varepsilon}$ (J/mol)	$2800 + 5\,T$	59
$\Delta G_{Si}^{\gamma\to\varepsilon}$ (J/mol)	$-560 - 8\,T$	59
$\Delta G_C^{\gamma\to\varepsilon}$ (J/mol)	$-22{,}166$	60
$\Delta\Omega_{FeMn}^{\gamma\to\varepsilon}$ (J/mol)	$2873 - 717(x_{Fe} - x_{Mn})$	59
$\Delta\Omega_{FeC}^{\gamma\to\varepsilon}$ (J/mol)	$42{,}500$	60
$\Delta\Omega_{FeSi}^{\gamma\to\varepsilon}$ (J/mol)	$2850 + 3520(x_{Fe} - x_{Si})$	59
$\Delta\Omega_{FeAl}^{\gamma\to\varepsilon}$ (J/mol)	3328	59
$\Delta\Omega_{MnC}^{\gamma\to\varepsilon}$ (J/mol)	$26{,}910$	60
G_{mg}^{φ} (J/mol)	$RTf(T/T_N^{\varphi})\ln(1 + \beta^{\varphi}/\mu_B), \quad \varphi = \gamma, \varepsilon$	59
$f(T/T_\varphi^N)$	$1 - \dfrac{\frac{79\tau^{-1}}{140p} + \frac{474}{497}(\frac{1}{p} - 1)(\frac{\tau^3}{6} + \frac{\tau^9}{135} + \frac{\tau^{15}}{600})}{D},$ when $\tau \leq 1\,(\tau = T/T\varphi\,N)$; $-\dfrac{\left(\frac{t^{-5}}{10} + \frac{t^{-15}}{315} + \frac{t^{-25}}{1500}\right)}{D}$, when $\tau > 1$	59
D	$\frac{518}{1125} + \frac{11692}{15975}(\frac{1}{p} - 1),\; p = 0.28$	59
β^{γ}/μ_B (J/mol)	$0.7x_{Fe} + 0.62x_{Mn} - 0.64x_{Fe}x_{Mn} - 4x_C$	61
$\beta^{\varepsilon}/\mu_B$ (J/mol)	$0.62x_{Mn} - 4x_C$	61
T_N^{γ} (K)	$251.71 + 681x_{Mn} - 1575x_{Si} - 1740x_C$	59
T_N^{ε} (K)	$580x_{Mn}$	59

where x_i, $\Delta G_i^{\gamma\to\varepsilon}$, $\Delta\Omega_{ij}^{\gamma\to\varepsilon}$, and $\Delta G_{mg}^{\gamma\to\varepsilon}$ show the molar fraction, free energy change, the interaction energy between the components i and j, and the free energy contribution due to the magnetic transition, respectively. T, β^{φ}, $T\varphi\,N$, μ_B are temperature, magnetic moment, Néel temperature, and Bohr magneton, respectively. a, R, and N are lattice parameter of austenite, gas constant and Avogadro constant.

brittle fracture. Therefore, the inclusions observed in this study (Figure 11(a4)) also would assist the deterioration of cryogenic ductility. However, initiations of numerous damages were observed in the region without inclusions, and the brittle fracture did not occur instantaneously (crack arrest in ferrite). Hence, the presence of inclusions is not the major factor for the tensile-deformation-induced brittle fracture in the present study. Therefore, the martensite-related micro-damage mechanisms is key to understanding the temperature effects on the fracture behavior and associated mechanical properties.

C. Micro-damage Mechanisms

For the specimen tested at 297 K and 373 K (24 °C and 100 °C), the micro-damage initiated and propagated within deformation-induced martensite or its interface, which was attributed to stress concentration at martensite due to the high strength and strain incompatibility.[43,66] The initiated micro-damage was arrested when it grew to ferrite as shown in Figure 13. As a result, the micro-damage size initially increased with strain due to slight propagation to ferrite and the damage tip blunting, and then became constant (Figure 12). In other words, a factor determining the

damage size was the size of deformation-induced martensite. These results indicated that ferrite played a role in damage arrest during deformation. The completely blunt damage became void; accordingly, the shallow dimples appeared on the fracture surfaces, whose size corresponded to the damage size observed in the region of deformation-induced martensite. It is also noteworthy that the average damage size after the occurrence of the damage arrest was not dependent on deformation temperature (i.e., within a range of 1.5 to 2.1 μm^2, irrespective of temperature). This result indicates that the damage initiation size was deformation-induced martensite even at 243 K and 173 K. The variation trend of the number density of damage with temperature is also noticeable for understanding damage initiation behavior (Figure 12). The number density of damage indicates a significant increase in the micro-damage initiation probability at each strain. Because the preferential damage initiation site was deformation-induced martensite at all temperature, the promotion of TRIP by decreasing temperature acted as a factor increasing damage initiation probability. Moreover, the increase in flow stress with decreasing temperature provides a larger mechanical driving force for the brittle damage initiation. That is, the temperature dependence of damage initiation behavior mainly
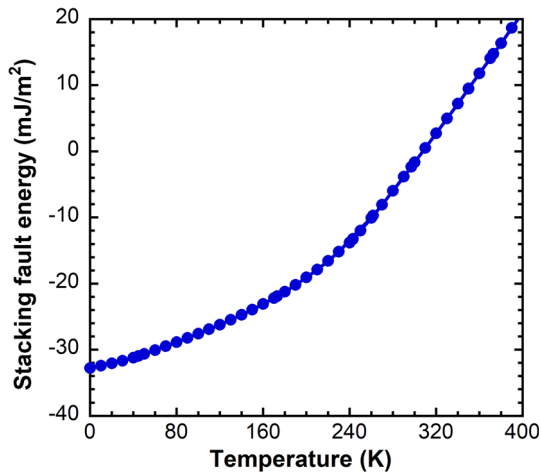
Fig. 16—SFE as a function of temperature in the retained austenite.

resulted from the increase in flow stress, and the decrease in the austenite stability.

However, the fracture surface was totally changed with decreasing temperature. As mentioned above, when the initiated damage is fully arrested via its tip blunting, the fracture surface shows shallow dimples. Therefore, the appearance of quasi-cleavage fracture feature on the fracture surfaces at 243 K and 173 K indicates that the micro-damage arrestability of ferrite was deteriorated by decreasing temperature. The primary reason for the deterioration of micro-damage arrestability in ferrite is the increase in flow stress with decreasing temperature, which allows to reach critical stress or stress intensity factor for brittle cracking.

Moreover, the increase in flow stress by decreasing temperature also assists brittle cracking at martensite. As shown in Figure 6, the martensite was largely elongated, and showed ferrite/martensite laminated microstructure at the 0.4 strain at 173 K. Therefore, the promotion of martensite cracking enables crack propagation along the lamellar alignment, which thereby caused the crack propagation along with the crack propagation as shown in Figure 10. The crack propagation along the laminated microstructure stopped when its tip meets ferrite via crack tip blunting (Figure 15). However, as discussed above, the damage arrestability in ferrite was also deteriorated at 173 K. Therefore, the brittle fracture occurred and showed fully quasi-cleavage brittle fracture surface. It is also noticeable that the austenite of the present steel contains a high concentration of C, which caused the high flow stress and low stress accommodation capability in martensite. For instance, a Fe–Mn metastable austenitic alloy without C showed monotonic increases in strength and ductility with decreasing temperature.[25] Therefore, controlling C concentration in retained austenite, ferrite plasticity, and microstructure distribution are key to designing the Fe–Mn-based cryogenic materials.

V. CONCLUSIONS

The temperature effects on the mechanical properties and damage evolution in a medium Mn steel were investigated. The following conclusions were drawn:

(1) At the deformation temperatures ranging from 173 K to 373 K (− 100 °C to 100 °C), UTS significantly decreased and UEl and TEl increased with increasing temperature, of which the trend was determined by the necking condition. Moreover, the difference between UEl and TEl, *i.e.*, post-uniform elongation, was within 2 to 4 pct, which indicates that the final fracture occurred after only a small amount of plasticity evolution, irrespective of temperature.

(2) The small post-uniform elongation was attributed to the formation of numerous micro-damage such as crack and void. The damage formed within deformation-induced martensite and at the ferrite/martensite interfaces, and thus decreasing temperature increased the damage initiation probability and decreased critical strain for the damage initiation.

(3) After the martensite cracking, the surrounding ferrite grains suddenly underwent a high stress or stress intensity factor particularly in cryogenic temperature. Therefore, decreasing temperature also deteriorated the micro-damage arrestability of ferrite through the occurrence of transgranular brittle cracking.

(4) The fracture mode changed with decreasing temperature from ductile to quasi-cleavage fractures. The occurrence of the fully quasi-cleavage fracture indicated that the crack initiation at martensite and subsequent brittle crack growth into ferrite were the predominant feature in the fracture process at the cryogenic temperature. Hence, it was concluded that the deformation-induced martensite, which is intrinsically important for TRIP effect, plays dual roles in brittle fracture of the medium Mn steel in cryogenic temperature.

CONFLICT OF INTEREST

On behalf of all authors, the corresponding author states that there is no conflict of interest.

REFERENCES

1. Y.K. Lee and J. Han: *Mater. Sci. Technol.*, 2015, vol. 31, pp. 843–56.
2. D.W. Suh, J.H. Ryu, M.S. Joo, H.S. Yang, K. Lee, and H.K.D.H. Bhadeshia: *Metall. Mater. Trans. A*, 2013, vol. 44A, pp. 286–93.
3. J.T. Benzing, A. Kwiatkowski da Silva, L. Morsdorf, J. Bentley, D. Ponge, A. Dutta, J. Han, J.R. McBride, B. Van Leer, B. Gault, D. Raabe, and J.E. Wittig: *Acta Mater.*, 2019, vol. 166, pp. 512–30.
4. T.W.J. Kwok, K.M. Rahman, X. Xu, I. Bantounas, J.F. Kelleher, S. Dasari, T. Alam, R. Banerjee, and D. Dye: *Mater. Sci. Eng. A*, 2020, vol. 782, 139258.
5. H. Choi, S. Lee, J. Lee, F. Barlat, and B.C. De Cooman: *Mater. Sci. Eng. A*, 2017, vol. 687, pp. 200–10.
6. K. Steineder, D. Krizan, R. Schneider, C. Béal, and C. Sommitsch: *Steel Res. Int.*, 2018, vol. 89, pp. 2–7.
7. K.I. Sugimoto, H. Tanino, and J. Kobayashi: *Steel Res. Int.*, 2015, vol. 86, pp. 1151–60.
8. S. Lee, Y. Estrin, and B.C. De Cooman: *Metall. Mater. Trans. A*, 2013, vol. 44A, pp. 3136–46.
9. S. Lee, S.H. Kang, J.H. Nam, S.M. Lee, J.B. Seol, and Y.K. Lee: *Metall. Mater. Trans.*, 2019, vol. 50, pp. 2655–64.
10. S.Y. Han, S.Y. Shin, H.J. Lee, B.J. Lee, S. Lee, N.J. Kim, and J.H. Kwak: *Metall. Mater. Trans. A*, 2012, vol. 43A, pp. 843–53.
11. T. Furukawa, H. Huang, and O. Matsumura: *Mater. Sci. Technol.*, 1994, vol. 10, pp. 964–70.
12. J.T. Benzing, W.E. Luecke, S.P. Mates, D. Ponge, D. Raabe, and J.E. Wittig: *Mater. Sci. Eng. A*, 2021, vol. 803, 140469.
13. D.M. Field, L.G. Garza-Martinez, and D.C. Van Aken: *Metall. Mater. Trans. A*, 2020, vol. 51A, pp. 4427–33.
14. C.Y. Lee, J. Jeong, J. Han, S.J. Lee, S. Lee, and Y.K. Lee: *Acta Mater.*, 2015, vol. 84, pp. 1–8.
15. C. Wang, W. Cao, J. Shi, C. Huang, and H. Dong: *Mater. Sci. Eng. A*, 2013, vol. 562, pp. 89–95.
16. H. Huang, O. Matsumura, and T. Furukawa: *Mater. Sci. Technol.*, 1994, vol. 10, pp. 621–26.
17. S.J. Lee, Y.M. Park, and Y.K. Lee: *Mater. Sci. Eng. A*, 2009, vol. 515, pp. 32–37.
18. E. De Moor, D.K. Matlock, J.G. Speera, and M.J. Merwin: *Scr. Mater.*, 2011, vol. 64, pp. 185–88.
19. H. Luo, J. Shi, C. Wang, W. Cao, X. Sun, and H. Dong: *Acta Mater.*, 2011, vol. 59, pp. 4002–14.
20. Z.H. Cai, H. Ding, R.D.K. Misra, and Z.Y. Ying: *Acta Mater.*, 2015, vol. 84, pp. 229–36.
21. Q. Tonizzo, M. Mazière, A. Perlade, and A.F. Gourgues-Lorenzon: *J. Mater. Sci.*, 2020, vol. 55, pp. 9245–57.
22. Q. Tonizzo, A.F. Gourgues-Lorenzon, M. Mazière, A. Perlade, and I. Zuazo: *Mater. Sci. Eng. A*, 2017, vol. 706, pp. 217–26.
23. A. Dutta, D. Ponge, S. Sandlöbes, and D. Raabe: *Materialia*, 2019, vol. 5, 100252.
24. Y. Ma, B. Sun, A. Schökel, W. Song, D. Ponge, D. Raabe, and W. Bleck: *Acta Mater.*, 2020, vol. 200, pp. 389–403.
25. J.S. Kim, J.B. Jeon, J.E. Jung, K.K. Um, and Y.W. Chang: *Met. Mater. Int.*, 2014, vol. 20, p. 20.
26. J. Han, A.K. da Silva, D. Ponge, D. Raabe, S.M. Lee, Y.K. Lee, S.I. Lee, and B. Hwang: *Acta Mater.*, 2017, vol. 122, pp. 199–206.
27. I.C. Yi, Y. Ha, H. Lee, A. Zargaran, and N.J. Kim: *Met. Mater. Int.*, 2017, vol. 23, pp. 283–89.
28. M.T. Kim, T.M. Park, K.H. Baik, W.S. Choi, P.P. Choi, and J. Han: *Acta Mater.*, 2019, vol. 164, pp. 122–34.
29. M. Kuzmina, D. Ponge, and D. Raabe: *Acta Mater.*, 2015, vol. 86, pp. 182–92.
30. J. Chen, M. Lv, S. Tang, Z. Liu, and G. Wang: *Mater. Char.*, 2021, vol. 106, pp. 108–11.
31. M. Koyama, T. Lee, C.S. Lee, and K. Tsuzaki: *Mater. Des.*, 2013, vol. 49, p. 49.
32. H. Kim, Y. Ha, K.H. Kwon, M. Kang, N.J. Kim, and S. Lee: *Acta Mater.*, 2015, vol. 87, p. 87.
33. V. Shterner, I.B. Timokhina, and H. Beladi: *Mater. Sci. Eng. A*, 2016, vol. 669, pp. 437–46.
34. O. Umezawa and K. Nagai: *Metall. Mater. Trans. A*, 1998, vol. 29A, pp. 809–22.
35. T.S. Byun, N. Hashimoto, and K. Farrell: *Acta Mater.*, 2004, vol. 52, pp. 3889–99.
36. K. Barat, H.N. Bar, D. Mandal, H. Roy, S. Sivaprasad, and S. Tarafder: *Mater. Sci. Eng. A*, 2014, vol. 597, pp. 37–45.
37. L.X. Zhou and T.N. Baker: *Mater. Sci. Eng. A*, 1994, vol. 177, pp. 1–9.
38. S.K. Lawrence, Y. Yagodzinskyy, H. Hänninen, E. Korhonen, F. Tuomisto, Z.D. Harris, and B.P. Somerday: *Acta Mater.*, 2017, vol. 128, pp. 218–26.
39. F. Otto, A. Dlouhý, C. Somsen, H. Bei, G. Eggeler, and E.P. George: *Acta Mater.*, 2013, vol. 61, pp. 5743–55.
40. Y.H. Jo, S. Jung, W.M. Choi, S.S. Sohn, H.S. Kim, B.J. Lee, N.J. Kim, and S. Lee: *Nat. Commun.*, 2017, vol. 8, pp. 1–8.
41. B. Gludovatz, A. Hohenwarter, K.V.S. Thurston, H. Bei, Z. Wu, E.P. George, and R.O. Ritchie: *Nat. Commun.*, 2016, vol. 7, pp. 1–8.
42. R.L. Miller: *Metall. Trans.*, 1972, vol. 3, pp. 905–12.
43. M. Koyama: *Acc. Mater. Res.*, 2021, vol. 2, pp. 1167–76.
44. M. Koyama, C. Cem, E. Akiyama, and K. Tsuzaki: *Acta Mater.*, 2014, vol. 70, pp. 174–87.
45. V.K. Verma, M. Koyama, S. Hamada, and E. Akiyama: *Mater. Sci. Eng. A*, 2020, vol. 782, 139250.
46. C.X. Hao, M. Koyama, and E. Akiyama: *Metall. Mater. Trans. A*, 2020, vol. 51A, pp. 6184–94.
47. Y.T. Zhou, T. Hojo, M. Koyama, and E. Akiyama: *Mater. Sci. Eng. A*, 2021, vol. 819, 141479.
48. J. Han, S.J. Lee, J.G. Jung, and Y.K. Lee: *Acta Mater.*, 2014, vol. 78, pp. 369–77.
49. K. Steineder, D. Krizan, R. Schneider, C. Béal, and C. Sommitsch: *Acta Mater.*, 2017, vol. 139, pp. 39–50.
50. A. Müller, C. Segel, M. Linderov, A. Vinogradov, A. Weidner, and H. Biermann: *Metall. Mater. Trans. A*, 2016, vol. 47A, pp. 59–74.
51. J.J. Jonas, R.A. Holt, and C.E. Coleman: *Acta Metall.*, 1976, vol. 24, pp. 911–18.
52. S. Lee and K. Park: *Metall. Mater. Trans. A*, 2013, vol. 44A, pp. 3423–27.
53. R. Kakimoto, M. Koyama, and K. Tsuzaki: *ISIJ Int.*, 2019, vol. 59, pp. 2334–42.
54. M. Eskandari, A. Hanzaki, M.A. Bonab, Y. Onuki, R. Basu, A. Asghari, and J.A. Szpunar: *Mater. Sci. Eng. A*, 2016, vol. 674, pp. 514–28.
55. T.S. Byun: *Acta Mater.*, 2003, vol. 51, pp. 3063–71.
56. S. Lee and B.C. De Cooman: *Metall. Mater. Trans. A*, 2014, vol. 45A, pp. 709–16.
57. J.A. Castañeda, O.A. Zambrano, G.A. Alcázar, S.A. Rodríguez, and J.J. Coronado: *Metals*, 2021, vol. 11, pp. 1701–20.
58. G.B. Olson and M. Cohen: *Metall. Trans. A*, 1976, vol. 7A, pp. 1915–23.
59. S. Curtze, V.T. Kuokkala, A. Oikari, J. Talonen, and H. Hänninen: *Acta Mater.*, 2011, vol. 59, pp. 1068–76.
60. S. Allain, J.P. Chateau, O. Bouaziz, S. Migot, and N. Guelton: *Mater. Sci. Eng. A*, 2004, vol. 387–389, pp. 158–62.
61. A.S. Akbari, J. Imlau, U. Prahl, and W. Bleck: *Metall. Mater. Trans. A*, 2009, vol. 40A, pp. 3076–90.
62. C.P. Scott and J. Drillet: *Scripta Mater.*, 2007, vol. 56, pp. 489–92.
63. M. Koyama, T. Yamashita, S. Morooka, T. Sawaguchi, Z. Yang, T. Hojo, T. Kawasaki and S. Harjo: ISIJ Int., 2022, vol. 62, pp. 2036–42.
64. M. Koyama, Y. Shimomura, A. Chiba, E. Akiyama, and K. Tsuzaki: *Scripta Mater.*, 2017, vol. 141, pp. 20–23.
65. R.S. Varanasi, M. Koyama, Y. Shibayama, and E. Akiyama: *Mater. Sci. Eng. A*, 2022, vol. 857, 144021.
66. M. Calcagnotto, Y. Adachi, D. Ponge, and D. Raabe: *Acta Mater.*, 2011, vol. 59, pp. 658–70.